Author(s):   Jensen, Thomas N. & Meinander, Kristoffer & Helveg, Stig & Foster, Adam S. & Kulju, Sampo & Musso, Tiziana & Lauritsen, Jeppe V.

Title: Atomic Structure of a Spinel-Like Transition Al2O3(100) Surface

Year: 2014

Version: Final published version

Atomic Structure of a Spinel-Like Transition Al$_2$O$_3$(100) Surface

Thomas N. Jensen,[1] Kristoffer Meinander,[1] Stig Helveg,[2] Adam S. Foster,[3] Sampo Kulju,[4]
Tiziana Musso,[3] and Jeppe V. Lauritsen[1,*]

[1]*Interdisciplinary Nanoscience Center (iNANO), Aarhus University, Gustav Wieds Vej 14, DK-8000 Aarhus C, Denmark*
[2]*Haldor Topsøe A/S, Nymøllevej 55, DK-2800 Kgs. Lyngby, Denmark*
[3]*COMP, Department of Applied Physics, Aalto University, Otakaari 1, FI-00076 Aalto, Finland*
[4]*Department of Physics, Tampere University of Technology, P.O. Box 692, FI-33010 Tampere, Finland*

We study a crystalline epitaxial alumina thin film with the characteristics of a spinel-type transition Al$_2$O$_3$(100) surface by using atom-resolved noncontact atomic force microscopy and density functional theory. It is shown that the films are terminated by an Al-O layer rich in Al vacancies, exhibiting a strong preference for surface hydroxyl group formation in two configurations. The transition alumina films are crystalline and perfectly stable in ambient atmospheres, a quality which is expected to open the door to new fundamental studies of the surfaces of transition aluminas.

Because of its excellent thermal and mechanical stability, alumina (Al$_2$O$_3$) is a key material in many coatings, ceramics, and adsorbents, and it is the most widely used support for catalyst particles in heterogeneous catalysis [1–3]. In addition to the crystalline, nonporous α-Al$_2$O$_3$ (corundum), numerous metastable polymorphs of alumina have been identified, e.g., γ-, δ-, and η-Al$_2$O$_3$ [4,5]. A key characteristic of industrial alumina is that the material can be produced as a nanocrystalline powder material with a very high surface area (50–300 m^2/g for γ-Al$_2$O$_3$). Especially the γ-Al$_2$O$_3$ phase is a useful support for a wide range of heterogeneous catalysts [3,6,7] and as a catalyst with an acido-basic function [8]. Despite the strong importance of transition aluminas, the crystal structure of the most porous of the alumina types is still being debated intensively, and their actual atomic scale surface structure remains distinctly undetermined. It has so far not been possible to obtain single crystals of the transition aluminas large enough for surface science studies, which further complicates the characterization of these insulating surfaces. The bulk crystal phases of the γ-, δ-, and η-Al$_2$O$_3$ polymorphs (here denoted s-Al$_2$O$_3$ in short) are often described starting from a defective spinel-like ($A^{2+}B_2^{3+}O_4^{2-}$) structure where Al is the only cation and positioned in tetrahedral (T_d) and octahedral (O_h) sites [2,9,10]. In order to keep the Al$_2$O$_3$ stoichiometry, 11.1% Al vacancies must be introduced, resulting in an alumina unit cell with two Al vacancies per 24 O ions (Al$_{16}$O$_{24}$ vs Mg$_6$Al$_{12}$O$_{24}$). The main difference between the γ-, δ-, and η-Al$_2$O$_3$ polymorphs is often regarded to lie in the distribution of the Al and Al vacancies among O_h and T_d sites [4]. The Al distribution is controversial though, and recent theoretical work focused on γ-Al$_2$O$_3$, on the other hand, described the s-Al$_2$O$_3$ polymorph by a spinel-like oxygen face-centered-cubic (fcc) lattice where the Al distribution involved nonspinel sites [11].

All transition alumina surfaces are known to become highly hydroxylated, and under most relevant conditions γ-Al$_2$O$_3$ has 10–15 OH groups/nm^2 [3]. Linear OH groups adsorbed on penta-coordinated Al (OH-Al$_{penta}$) are attributed to Brønsted bases, while bridged OH groups adsorbed on lattice O atoms (H-O$_{lattice}$) are assigned to Brønsted acids. After dehydroxylation of the surface, it develops Lewis acidity on the uncoordinated Al$_{penta}$ sites. A recent study highlighted these Lewis-acidic Al$_{penta}$ on the (100) surface of γ-Al$_2$O$_3$ as sites with a particularly strong affinity for anchoring Pt [12]. The nature and location of such surface sites and their interaction with metallic particles and adsorbates are thus issues of key importance [13]. So far, the most valuable atomic-scale information on the Al-O coordination of alumina surfaces has been obtained from alumina ultrathin films on NiAl [14–18] or by noncontact atomic force microscopy (NC-AFM) on an α-Al$_2$O$_3$ single crystal [19,20]. However, no satisfactory model for the surface of an insulating s-Al$_2$O$_3$ phase has emerged. Here we successfully demonstrate that a perfectly crystalline (100)-oriented transition alumina film with a defective spinel structure representative of a bulk transition alumina can be realized by pseudomorphic growth on a spinel MgAl$_2$O$_4$(100) surface and imaged in atomic detail with NC-AFM, which in recent years has become a primary tool for the atomic-scale analysis of insulator surfaces.

Preparation of the MgAl$_2$O$_4$(100) surface requires ion sputtering and annealing to 1200 °C in 10^{-7} mbar O$_2$ (see [21] for a detailed description of the experimental methods). NC-AFM images were recorded in ultrahigh vacuum (UHV) at pressures below 10^{-10} mbar by oscillating a silicon cantilever with constant amplitude. Al was evaporated by means of physical vapor deposition from a high-purity Al rod (99.999 at.%), and the flux rate was 0.2 ML/min, as checked with NC-AFM. For x-ray

photoelectron spectroscopy (XPS) experiments, Al K_α radiation was used. All calculations in this work were performed by using the periodic plane-wave basis VASP code [22,23], implementing the spin-polarized density functional theory (DFT) and the generalized gradient approximation [24]. Projected augmented wave potentials were used to describe the core electrons [25]. In order to predict surface terminations, we use the calculated surface energy as an indicator, with lower energies predicting more stable surfaces. For nonstoichiometric surfaces, the surface energy depends on the temperature and partial pressures of the surrounding gas atmosphere (O_2 and H_2), and we have applied the chemical potential formalism [21,26,27].

The unit cell of the so-called normal spinel crystal phase AB_2O_4 has an fcc sublattice of oxygen ions with 1/3 of the cations (type A) in T_d and 2/3 (type B) in O_h interstices (Fig. 1 in [21]). The oxygen ions are positioned in rows, the directions of which alternate through the layers of the crystal repeating itself in an *abab* manner [Fig. 1(a)]. The atomic-scale structure of the $MgAl_2O_4(100)$ surface has been revealed by an interplay of atom-resolved NC-AFM, surface x-ray diffraction, and DFT [28,29], and the surface was shown to expose fivefold Al-terminated species (Al_{penta}) and a partly hydroxylated layer on the (100) surface [30]. The epitaxial mismatch between the $MgAl_2O_4(100)$ surface and the (100) surface of the s-Al_2O_3 types is less than 2% [31], suggesting that epitaxial growth of oxidized Al should promote the formation of a spinel-like alumina (s-Al_2O_3) phase [Fig. 1(b)].

The synthesis of alumina films in various O_2 pressure and temperature conditions has been explored. Prior to every synthesis, the $MgAl_2O_4(100)$ surface was cleaned until NC-AFM images showed an atomically flat surface with terrace widths exceeding several hundred nanometers [Fig. 2(a)]. The most optimum synthesis procedure, leading to a homogeneous and crystalline film, involved deposition of Al onto the freshly prepared $MgAl_2O_4(100)$ substrate in UHV and at room temperature. This was followed by postannealing of the Al particles in 10^{-7} mbar O_2 to 1200 °C (see Fig. 2 in [21] for NC-AFM images recorded after flash annealing temperatures ranging from 400 to 1200 °C in 10^{-7} mbar O_2). At annealing temperatures of 1200 °C, crystalline islands started to form on the substrate terraces. In order to study the morphology of these islands as a function of surface coverage, a series of samples with coverages ranging from 0.4 to 4 ML were prepared [Fig. 2].

The submonolayer elongated ≈ 50 nm wide islands are atomically flat and are distinguishable [Fig. 2(b)] from the substrate by the island size compared to pristine $MgAl_2O_4(100)$ terraces. Furthermore, the islands have a more irregular perimeter and a preferred island growth direction along only one of the two high-symmetry directions of the substrate [Fig. 1]. Additional Al leads to a more complete film covering the entire surface [Fig. 2(c)]. At a surface coverage equivalent to 4 ML [Fig. 2(d)], the surface morphology is more diverse with triple-layer rectangular islands (islands with a height of three alumina layers) formed on top of closed alumina film layers. A step height analysis of the alumina islands in the NC-AFM images shows that the three most frequent step heights are in good correspondence with single (2.02 Å), double, and triple step heights in the spinel structure (Fig. 3 in [21]).

The rectangular geometry of the islands and the preferential 90° alternation of the rectangles in each layer [Fig. 2(d)] is expected for patches with a spinel-like alumina structure (s-Al_2O_3), due to the 90° alternation of the Al_{penta} rows exposed in subsequent (100) layers in the spinel structure [Fig. 1(b)] [30]. This observation clearly shows that the film coherently adopts a crystalline spinel structure and not a corundum structure, which would normally be expected at this high synthesis temperature. Corundum crystallizes in the tetragonal crystal system, making it unlikely that it would form rectangular islands on $MgAl_2O_4(100)$. The presence of smaller rectangular islands on top of closed layers may indicate that the strain induced by the lattice mismatch between $MgAl_2O_4(100)$ and the s-Al_2O_3 film is gradually relieved as a function of alumina film coverage, in correspondence with the Stranski-Krastanov growth mechanism [32].
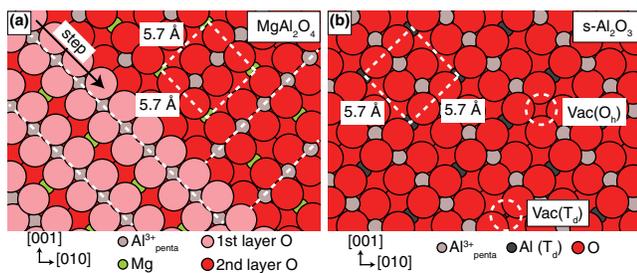

FIG. 1 (color online). Top view ball models of the (a) $MgAl_2O_4(100)$ and (b) s-$Al_2O_3(100)$ surfaces. Surface unit cells, high symmetry directions, and Al vacancies are marked with dashed lines.
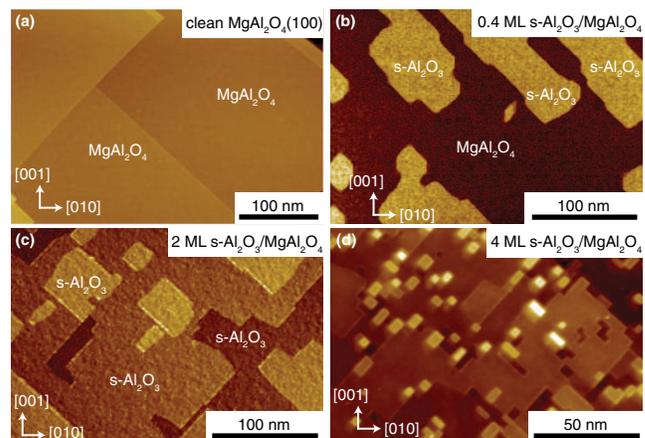

FIG. 2 (color online). NC-AFM images of (a) a $MgAl_2O_4(100)$ surface and (b)–(d) $Al/MgAl_2O_4(100)$ surfaces with increasing Al coverage.

Alternatively, the formation of smaller islands can be seen as the onset of growth of a more porous film, in accordance with the expected nature of s-Al_2O_3. At a surface coverage of > 10 ML, a comparatively rough surface resulted, indicating that the epitaxial confinement of the Al_2O_3 is lost (see Fig. 4 in [21]).

To follow more closely the steps involved in the oxidation of the deposited Al, a series of syntheses were performed where Al equivalent to a 4 ML s-Al_2O_3 film was sequentially annealed to increasing temperatures (100–1200 °C) in 10^{-7} mbar O_2 and then characterized with XPS [Fig. 3(a)]. Al was initially found in the two expected oxidation states: Al^{3+} (from Al in $MgAl_2O_4$) and Al^0 (from metallic Al on the surface). The oxidation states can be distinguished because the binding energy for Al^0 is ≈ 2.5 eV lower with respect to the binding energy of Al^{3+} [33]. At a temperature as low as 400 °C, XPS showed that all Al^0 was oxidized into Al^{3+}. At this stage the NC-AFM images revealed a rather rough surface consisting of many small particles distributed on the surface (Fig. 2 in [21]). The particles have a size of approximately 5 nm and reflect rather small grains of Al_2O_3 with an amorphous structure and no epitaxial relation to the substrate. As the temperature is increased, the Al_2O_3 particle size decreases (in both height and diameter) and the particle density decreases from 55 particles/(100 nm^2) at room temperature to 33 particles/(100 nm^2) at 800 °C (Fig. 5 in [21]). At this temperature, the $MgAl_2O_4(100)$ substrate is expected to dehydroxylate completely and expose a strongly interacting Al_{penta} terminated surface [Fig. 1(a)] which enables a strong interaction with the alumina particles [27]. The process is thus equivalent to sintering of alumina powder during calcination, and the decrease in particle density and size is interpreted as a partial conversion of the Al_2O_3 grains into an epitaxial film. The NC-AFM data show that annealing to 900–1000 °C is needed to form a fully crystalline film with the characteristic rectangular islands, showing that they have adapted a spinel-like structure. Further annealing to 1200 °C shows that the smaller rectangular s-Al_2O_3 islands have sintered into larger, coherent, and fully crystalline facets in agreement with the morphology in Fig. 2(c).
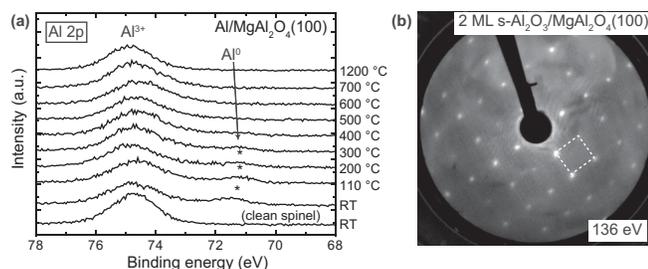
Despite the insulating nature, it was possible to perform low-energy electron diffraction (LEED) on the surface, which shows a perfectly crystalline surface reflected by sharp diffraction spots [Fig. 3(b)]. The peaks in the LEED image reflect the surface unit cell of the s-Al_2O_3 surface [Fig. 1(b)], and the measured dimensions in reciprocal space correspond to the square 5.7 Å × 5.7 Å surface unit cell cornered by T_d Al ions on the s-Al_2O_3 surface.

Figure 4 illustrates a zoomed-in partially atomically resolved NC-AFM image from one of the large facets of the s-Al_2O_3 film [Fig. 2(c)]. The NC-AFM image and its corresponding 2D Fourier transform reveals a crystalline surface with a periodic square lattice of protrusions, consistent with the symmetry of the (100) surface of s-Al_2O_3 spinel [Fig. 1(b)]. The square lattice is interrupted by a low concentration of point defects, which are imaged as 80 pm deep depressions in the surface. By superimposing a grid on the square lattice [Fig. 4(b)], it is observed that the defects all occupy the same positions in this lattice, suggesting they are of the same type. The defect density as determined by NC-AFM was 39 defects/(100 nm^2), which corresponds to a 12.6% vacancy concentration. This is in agreement with the aforementioned theoretical 11.1% vacancy concentration, which must be introduced in s-Al_2O_3 in order to keep the alumina stoichiometry in the spinel structure. The same type of single site depressions are not observed on the pristine $MgAl_2O_4(100)$ substrate [30], and we therefore tentatively associate these defects with the Al vacancies which are needed to stabilize Al_2O_3 in the (AB_2O_4) spinel structure.

To obtain a better understanding of the surface termination of the film and the possible distribution of the Al vacancies in the film layers and surface, the structure and energetics of uniform s-$Al_2O_3/MgAl_2O_4(100)$ systems were simulated by means of DFT calculations. In the
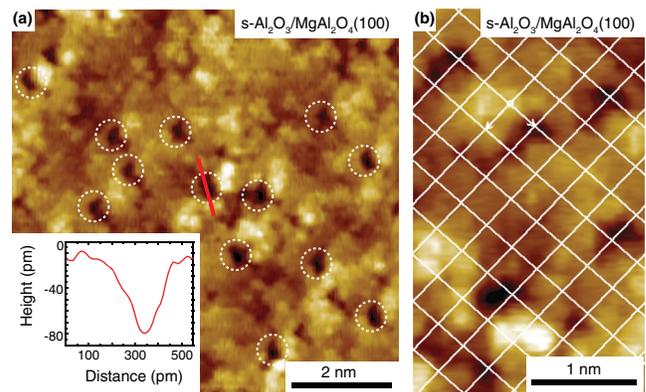

FIG. 4 (color online). Partially atom-resolved NC-AFM image of the s-$Al_2O_3(100)$ recorded in constant detuning mode with $df_{set} = -56$ Hz, $U_{bias} = -0.4$ V, and $A_{p-p} = 8$ nm. (a) Depressions are marked with dashed white circles, and the inset shows a line scan across one of these depressions. (b) Square lattice grid superimposed on the NC-AFM image.
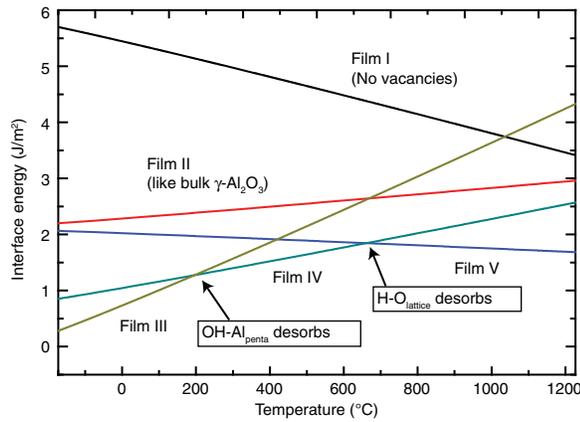

FIG. 3. (a) XPS spectra of the Al $2p$ region. (b) Normal incidence LEED pattern of s-$Al_2O_3(100)$.

FIG. 5 (color online).   Interface energy plot of the most relevant s-Al$_2$O$_3$ films with respect to the bulk MgAl$_2$O$_4$ structure. Film I, all vacancies are replaced with Al; film II, vacancies like bulk γ-Al$_2$O$_3$; films III–V, including adsorbed H and OH groups.

DFT calculations, we systematically considered the effect of film thickness, the concentration and distribution of Al vacancies, and the effect of adding surface OH groups and H on the O lattice. Figure 5 plots the interface energy of the most relevant 4 ML s-Al$_2$O$_3$ film configurations relative to the bulk MgAl$_2$O$_4$ structure, taking into account the chemical potentials of O$_2$ and H$_2$ at the experimental preparation conditions. All configurations of s-Al$_2$O$_3$ films regardless of structure and vacancy concentration in the 1–4 ML range were found to have a higher surface energy than the substrate reference, with the highest energy for the 4 ML films. This result is fully expected, since s-Al$_2$O$_3$ is a metastable phase, and is in agreement with experiments, where 1–2 ML step heights were more common and it was not possible to form a stable epitaxial system for s-Al$_2$O$_3$ films thicker than approximately 5 ML. The s-Al$_2$O$_3$ film gains stability by introducing Al vacancies with the same concentration and distribution as bulk γ-Al$_2$O$_3$. The Al vacancy concentration as determined by DFT is 8.6% for the most favorable films (III-V), which is in reasonable agreement with experiment [see Fig. 6 in [21] for a ball model of film (IV)].

The Al vacancy distributions in s-Al$_2$O$_3$ can, theoretically, range from all Al vacancies in T_d sites to all Al vacancies in O_h sites for the different spinel-like alumina phases [4]. In the bulk spinel-based transition alumina structure, the calculated relative energies of T_d and O_h vacancies with respect to α-Al$_2$O$_3$ show little difference between the stability of O_h and T_d vacancies (Fig. 7 in [21]). Calculations of the s-Al$_2$O$_3$/MgAl$_2$O$_4$(100) system suggest that both types of vacancy can be present in the lowest energy four layer structures, with a significant preference for O_h vacancies. Several studies suggest that δ-Al$_2$O$_3$ exclusively contains O_h vacancies, while η-Al$_2$O$_3$ has a strong preference for T_d vacancies. γ-Al$_2$O$_3$ is suggested to have both O_h and T_d vacancies with a

preference for O_h vacancies [4]. Thus, our DFT calculations indicate that the γ phase is representative for the synthesized s-Al$_2$O$_3$ films on MgAl$_2$O$_4$(100). Thinner alumina films of 1–2 ML, on the other hand, are destabilized by Al vacancies and are thereby not expected to represent the defective spinel structure very well.

The two simple (100) terminations obtained from a bulk truncation of spinel reflect a surface terminated by either a O$_4$-Al$_4$-O$_4$ layer with Al in O_h positions as in Fig. 1(b) or a surface terminated by Al in the T_d positions [shown in the subsurface of Fig. 1(b)]. The DFT results in Fig. 5 show that the bulk-truncated O$_4$-Al$_4$-O$_4$ terminated s-Al$_2$O$_3$(100) surface is strongly preferred in our case. Disregarding Al vacancies, the surface then consists of surface Al$_{penta}$ atoms in O_h sites and O double rows aligned in the [011] direction. The square geometry of the surface unit cell experimentally observed with LEED and NC-AFM is only seen when the lower tetrahedrally coordinated Al ions are noticed. Previous NC-AFM results for the MgAl$_2$O$_4$(100) surface which exposes the same Al and O surface termination showed that the effect of subsurface Mg is visible through the observation of a square unit cell at large tip-surface distances [27], and the observed square geometry in Fig. 4 is most likely due to the influence of the subsurface Al ions.

The DFT calculations furthermore predict that Al vacancies are more or less randomly dispersed throughout the film, both perpendicular to the surface and within layers, with a preference for at least some vacancies at the surface as seen in the NC-AFM experiment [Fig. 4]. The possibility of forming surface OH groups is interesting for the surface chemistry, and the calculations show that the 4 ML s-Al$_2$O$_3$ film incorporates H as surface OH groups in two configurations. At room temperature, OH sits directly on the Al$_{penta}$ rows, and additional H atoms can adsorb on the lattice O atoms forming another type of surface hydroxyl group (H-O$_{lattice}$). The OH-Al$_{penta}$ groups desorb around 200 °C, whereas the H-O$_{lattice}$ atoms are stable up to 660 °C [Fig. 5], which is in agreement with the dehydroxylation temperature of γ-Al$_2$O$_3$ [34]. The experimentally prepared surface in Fig. 4 was prepared above this temperature and is therefore not expected to reflect the fully hydroxylated situation. Nevertheless, H$_2$ and water are unavoidable rest gases in UHV, and we therefore speculate that the few bright spots in Fig. 4 reflect one or the other type of OH groups at a low coverage. The exact nature of such OH groups on the film will be investigated in future studies. Full hydroxylation is anticipated when the surface is exposed to a humid environment. To investigate the stability of the s-Al$_2$O$_3$ films in air, a film was studied with NC-AFM before and after air exposure for 4 hours (Fig. 8 in [21]). A comparison of NC-AFM images showed that neither the morphology nor roughness of the s-Al$_2$O$_3$ was altered by exposure to air.

In summary, well-defined, crystalline films have been successfully synthesized on atomically flat $MgAl_2O_4(100)$ substrates through oxidation of Al particles and experimentally characterized by means of NC-AFM, XPS, and LEED. As determined by NC-AFM, the crystalline islands have preferential growth directions along the high symmetry axes in the spinel structure, which strongly indicates that the islands have adapted the spinel-like structure of a transition alumina. This is supported by XPS results, which show that all Al^0 has been oxidized to Al^{3+}, and by LEED, where the measured surface unit cell in reciprocal space reflects the $5.7\ \text{Å} \times 5.7\ \text{Å}$ surface unit cell cornered by T_d Al ions on the s-Al_2O_3 surface. DFT calculations predict that s-Al_2O_3 films prefer an Al vacancy concentration similar to a transition alumina and, furthermore, that H and OH groups are favorably adsorbed on the surface, also indicating that the grown films adapt a spinel-like structure. Because of the high film stability in air shown in our study, it should be possible in future studies to perform a range of *ex situ* surface characterization experiments by, for example, infrared reflection-adsorption, Raman spectroscopy, and surface x-ray diffraction, and it opens for the possibility of carrying out *operando* measurements of well-characterized, supported metal catalysts on this model alumina surface. This may shed more light on the crucial role of alumina surfaces for the dispersion of active catalytic nanoparticles as well as the widespread use of dopants for sintering stability and moderators of surface chemical properties.

---

[*] jvang@inano.au.dk

[1] Z. Zhang, L. Li, and J. C. Yang, Acta Mater. **59**, 5905 (2011).

[2] G. N. Kryukova, D. O. Klenov, A. S. Ivanova, and S. V. Tsybulya, J. Eur. Ceram. Soc. **20**, 1187 (2000).

[3] I. Chorkendorff and J. W. Niemantsverdriet, in *Concepts of Modern Catalysis and Kinetics*, 2nd ed. (Wiley-VCH Verlag, Weinhem, 2007), pp. 190–196.

[4] C. Wolverton and K. C. Hass, Phys. Rev. B **63**, 024102 (2000).

[5] Z. Zhang and T. J. Pinnavaia, Angew. Chem., Int. Ed. **47**, 7501 (2008).

[6] M. W. Small, S. I. Sanchez, N. S. Marinkovic, A. I. Frenkel, and R. G. Nuzzo, ACS Nano **6**, 5583 (2012).

[7] O. Maresca, A. Allouche, J. P. Aycard, M. Rajzmann, S. Clemendot, and F. Hutschka, J. Mol. Struct. Theochem **505**, 81 (2000).

[8] P. Raybaud, M. Digne, P. Sautet, P. Euzen, and H. Toulhoat, J. Catal. **226**, 54 (2004).

[9] B. C. Lippens and J. H. Deboer, Acta Crystallogr. **17**, 1312 (1964).

[10] V. A. Ushakov and E. M. Moroz, React. Kinet. Catal. Lett. **24**, 113 (1984).

[11] M. Digne, P. Sautet, P. Raybaud, P. Euzen, and H. Toulhoat, J. Catal. **211**, 1 (2002).

[12] J. H. Kwak, J. Z. Hu, D. Mei, C. W. Yi, D. H. Kim, C. H. F. Peden, L. F. Allard, and J. Szanyi, Science **325**, 1670 (2009).

[13] W. Z. Li, L. Kovarik, D. H. Mei, J. Liu, Y. Wang, and C. H. F. Peden, Nat. Commun. **4**, 2481 (2013).

[14] R. M. Jaeger, H. Kuhlenbeck, H. J. Freund, M. Wuttig, W. Hoffmann, R. Franchy, and H. Ibach, Surf. Sci. **259**, 235 (1991).

[15] A. Stierle, F. Renner, R. Streitel, H. Dosch, W. Drube, and B. C. Cowie, Science **303**, 1652 (2004).

[16] S. Degen, A. Krupski, M. Kralj, A. Langner, C. Becker, M. Sokolowski, and K. Wandelt, Surf. Sci. **576**, L57 (2005).

[17] G. Kresse, M. Schmid, E. Napetschnig, M. Shishkin, L. Kohler, and P. Varga, Science **308**, 1440 (2005).

[18] G. H. Simon, M. Heyde, and H. J. Freund, J. Phys. Condens. Matter **24**, 084007 (2012).

[19] C. Barth and M. Reichling, Nature (London) **414**, 54 (2001).

[20] J. V. Lauritsen, M. C. R. Jensen, K. Venkataramani, B. Hinnemann, S. Helveg, B. S. Clausen, and F. Besenbacher, Phys. Rev. Lett. **103**, 076103 (2009).

[21] See Supplemental Material at http://link.aps.org/supplemental/10.1103/PhysRevLett.113.106103 for a detailed description of methods and supporting NC-AFM and DFT results.

[22] G. Kresse and J. Furthmüller, Comput. Mater. Sci. **6**, 15 (1996).

[23] G. Kresse and J. Furthmüller, Phys. Rev. B **54**, 11169 (1996).

[24] J. P. Perdew, K. Burke, and M. Ernzerhof, Phys. Rev. Lett. **77**, 3865 (1996).

[25] P. E. Blochl, Phys. Rev. B **50**, 17953 (1994).

[26] X. G. Wang, A. Chaka, and M. Scheffler, Phys. Rev. Lett. **84**, 3650 (2000).

[27] F. Federici Canova, A. S. Foster, M. K. Rasmussen, K. Meinander, F. Besenbacher, and J. V. Lauritsen, Nanotechnology **23**, 325703 (2012).

[28] M. K. Rasmussen, A. S. Foster, F. F. Canova, B. Hinnemann, S. Helveg, K. Meinander, F. Besenbacher, and J. V. Lauritsen, Phys. Rev. B **84**, 235419 (2011).

[29] M. K. Rasmussen, K. Meinander, F. Besenbacher, and J. V. Lauritsen, Beilstein J. Nanotechnol. **3**, 192 (2012).

[30] M. K. Rasmussen, A. S. Foster, B. Hinnemann, F. F. Canova, S. Helveg, K. Meinander, N. M. Martin, J. Knudsen, A. Vlad, E. Lundgren, A. Stierle, F. Besenbacher, and J. V. Lauritsen, Phys. Rev. Lett. **107**, 036102 (2011).

[31] Y. Sakashita and T. Yoneda, J. Catal. **185**, 487 (1999).

[32] E. Bauer, Z. Kristallogr. **110**, 372 (1958).

[33] J. F. Moulder, W. F. Stickle, P. E. Sobol, and K. D. Bomben, in *Handbook of X-ray Photoelectron Spectroscopy*, edited by J. Chastain (Perkin-Elmer, Eden Prairie, MN, 1992), pp. 54–55.

[34] J. Hietala, A. Root, and P. Knuuttila, J. Catal. **150**, 46 (1994).